X-ray spectroscopic methods for the diagnosis of laser-imploded targets (invited)

B. Yaakobi, O. Barnouin, M. C. Richardson, and J. M. Soures

Laboratory for Laser Energetics, University of Rochester, 250 East River Road, Rochester, New York 14623-1299

A. Hauer

Los Alamos National Laboratory, Los Alamos, New Mexico 87545

Benjamin Post

Polytechnic Institute of New York, Physics Department, Brooklyn, New York 11201

(Presented on 13 March 1986)

Several methods involving x-ray spectroscopic methods for diagnosing laser-imploded targets are discussed. The first method involves the recording of absorption lines formed in the target tamper, out of the continuum emitted by a hotter compressed core. This method is applied to ablatively imploded targets having a thin KCl signature layer. The tamper $\rho\Delta R$ is deduced from the area within the absorption lines, whereas the tamper temperature is deduced from the intensity distribution among absorption lines of adjacent charge states. In a second method, doubly diffracting crystals can give two-dimensional monochromatic images of thin signature layers in spherical targets. Such information is useful in studying stability and mixing. Experimental results relevant to these methods will be shown and the limitations on their application to laser-target experiments will be discussed.

I. X-RAY ABSORPTION LINES IN LASER-IMPLODED TARGETS

High temperatures ($\gtrsim 1$ keV) are often obtained in the central gas core of laser-imploded targets. Under these conditions, the continuous x-ray emission from the core passes out through the pusher and undergoes absorption at wavelengths characteristic of atomic species in the tamper. The resulting absorption lines can yield information on the temperature (T_e), density (ρ), and the $\rho\Delta R$ product (density times thickness) of the tamper. Particularly, strong absorption can be caused by resonance line transitions of the type $1s$-$2p$ in ions which have one or more vacancies in the $n = 2$ shell; these are thus inner-shell transitions. The optimal choice of tamper species for this method is such that at the prevailing tamper temperature, ionization will remove some of the L-shell ($n = 2$) electrons, as well as all electrons of higher shells. For the present experiment, potassium and chlorine bracketed the range of anticipated temperatures, and therefore a KCl absorption layer was embedded within the tamper. Chlorine and potassium absorption lines were indeed observed and used to determine the conditions within the KCl layer, and by inference, within the rest of the tamper.[1]

The targets used in this study (see Fig. 1) were imploded with the eight-beam Helios CO_2 laser system at the Los Alamos National Laboratory. The total laser energy was about 4.5 kJ in a pulse of a FWHM of about 650 ps. The imploded gas core reaches electron temperatures of about 700 eV, which excites a strong continuum around 3 keV (as well as 3–4-keV argon lines), which is a prerequisite for observing chlorine absorption lines. The relative position of the embedded KCl layer within the target is such that by the time of peak compression, most or all of the CH layer (but none of the KCl layer) has been ablated.

Figure 2 shows an example of the spectra emitted by these imploded targets. The contrast between strong Ar emission lines and strong Cl absorption lines vividly demonstrates a hot compressed core surrounded by a cooler shell.

Figure 3 shows in more detail the chlorine absorption structure. The identification of these line complexes was made by comparison with Hartree–Fock atomic structure calculations.[1] As an example, the line marked B in Fig. 3 corresponds to transitions of the type $1s$-$2p$ in boronlike chlorine (Cl^{+12}), i.e., $1s^22s^22p$-$1s2s^22p^2$; we likewise refer to other lines as the Be or the C feature, etc. For each configuration there can be several atomic states. For example, the B feature includes 14 transitions, the C feature contains 35 transitions.

The tamper temperature at the time of strong continuum emission from the core can be inferred from the intensi-

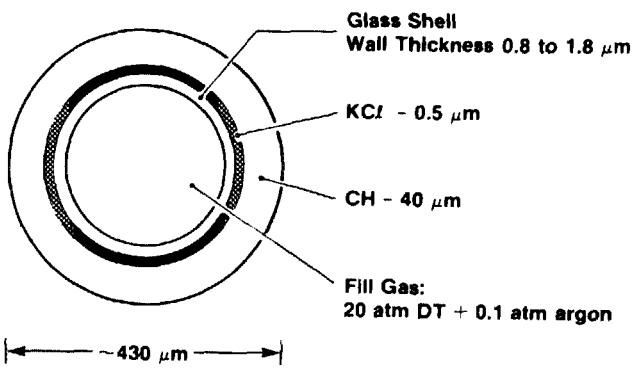

FIG. 1. Typical target parameters used in this experiment.

 0034-6748/86/082124-05$01.30

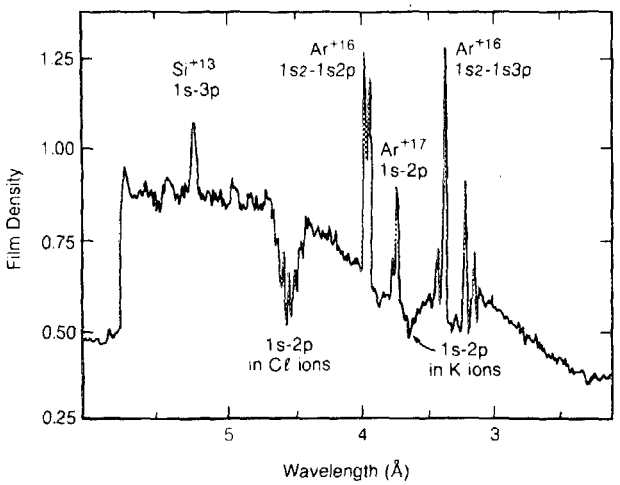

FIG. 2. Microdensitometer trace of a spatially resolved spectrum obtained from the target of Fig. 1.

ty ratios of the absorption features. The fact that the absorption features have a sharply peaked distribution of intensity is an indication that they are formed over a period of time when the tamper temperature does not vary appreciably. In order to estimate the tamper temperature from Fig. 3 we calculate the non-LTE steady-state distribution of chlorine charge states in a model which includes radiative, di-electronic, and three-body recombination, as well as ionization (collisional-radiative equilibrium model). The results (Fig. 4) show that this distribution depends primarily on the temperature and only slightly on the density in the range $(1–10)\times10^{23}$ cm^{-3}. For this density range the deduced temperature by comparison to Fig. 4 is in the range (200–230) eV.

The determination of the tamper $\rho\Delta R$ from the absorption lines is based on the cross section for photoabsorption on a spectral line of profile $\phi(\nu)$, normalized to total area of unity:

$$\sigma_\nu = (\pi e^2/mc) f\phi(\nu) = \sigma_0\phi(\nu), \tag{1}$$

where f is the absorption oscillator strength.

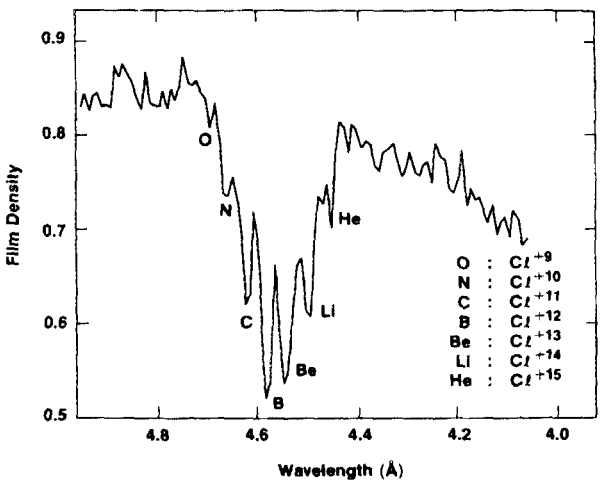

FIG. 3. Detailed tracing of the chlorine absorption lines of Fig. 2. The feature marked B corresponds to the transition $1s$-$2p$ in boronlike chlorine (Cl^{+12}), etc.

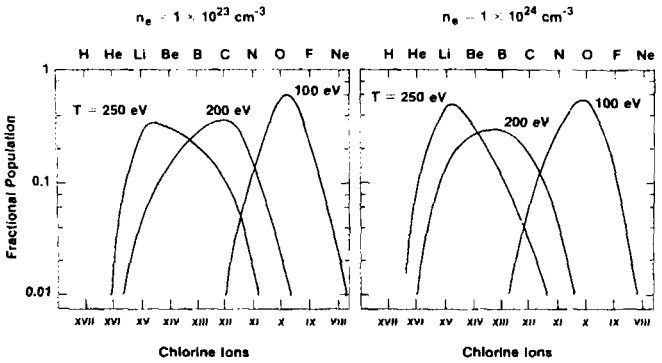

FIG. 4. Collisional-radiative model calculations of chlorine charge-state distribution at two densities. Smooth lines connect the calculated discreet points. Comparison of such curves to the spectrum of Fig. 3 is used to estimate the tamper temperature.

The attenuated intensity $I(\nu)$ through a layer of thickness ΔR and density ρ is related to the incident intensity I_0 (assumed independent of frequency) through

$$I(\nu) = I_0 \exp(-\sigma_\nu N_p \Delta R) = I_0 \exp(-\sigma_\nu \alpha\rho\Delta R/M_i), \tag{2}$$

where α is the fraction of all ions of ionization state p, whose density is N_p, which are in the ground state. The f value in Eq. (1) has to be averaged over the lower state levels as well as summed over the upper state levels. As examples, the Be ion has one ground state ($^1S_0$), the B ions—two ($^2P_{1/2}$, $^2P_{3/2}$).

The $\rho\Delta R$ can then be derived from the equation

$$\rho\Delta R = \left(\frac{M_i}{\sigma_0\alpha}\right)\int \ln\left(\frac{I_0}{I_\nu}\right) d\nu. \tag{3}$$

The integral is effectively over the line profile because the integrand vanishes far from the line center. In the approximation that the film density in Fig. 3 is exactly proportional to $\ln(I)$, this integral is simply the area enclosed within the absorption line. The total $\rho\Delta R$ of the KCl layer is given by the summation over the absorption line manifold such as that shown in Fig. 3. It is important to note that only the integral over the line profile is required for the determination of $\rho\Delta R$, so that the line profile need not be known.

Applying the procedure described here to the absorption lines of Fig. 3, following conversion from film density to intensity, overlapping lines deconvolution and integration, we derive a value of $\rho\Delta R = 5.1\times10^{-4}$ g/cm^2 for the KCl layer.

We used the LASNEX laser fusion code in a one-dimensional mode to simulate these experiments. At the time of peak core temperature, which should be about the time of peak core emission of continuum, the temperature in the KCl layer is 250 eV, in good agreement with the range (200–230) eV determined from the experiment. It should be pointed out that the predicted preheat temperature is only about 80 eV. The additional rise in tamper temperature is due to heat flowing outwards from the hot fill gas as well as due to the recompression of the expanded tamper. At the time of peak emission, the $\rho\Delta R$ of the KCl layer is about 10^{-3} g/cm^2, which is about twice the experimentally derived value. The sources of this difference between theory and experi-

ment include: (a) inaccuracy in the measurement of the background and continuum levels; (b) error due to time integration effects; and (c) error in the simulation itself, such as the hot electron transport methods. We can infer from this, by using the computational results, that the total $\rho\Delta R$ of the tamper at the time of peak emission was about 3.2×10^{-3} g/cm^2.

In order to directly simulate the absorption spectra, multigroup opacity tables were generated using the OPLIB opacity library (LTE). The resulting opacity tables were then used on line, as part of the LASNEX simulation. In Fig. 5 we show the results of the spectral simulation corresponding to the specific implosion that produced the spectrum in Fig. 2. OPLIB opacities were used only for the KCl layer. Argon emission was calculated with the average ion non-LTE opacity routine in LASNEX. Fine spectral resolution was used in the regions around the chlorine and potassium features and coarse resolution elsewhere. The depth of the absorption features in the simulation is similar to that observed in the experimental spectrum. The distribution of charge states in the simulation is somewhat different than in the experiment. This is mainly because the LTE assumption in OPLIB increases the ionization to higher charge states than predicted by a non-LTE model for the same temperature. It should be emphasized that the derivation of pusher temperature proceeds by comparing the measured spectrum to the non-LTE curves of Fig. 4, without reference to a hydrodynamic code. The LASNEX results are shown in order to demonstrate the ability to replicate the very existence of absorption lines in the spectrum. This satisfying result shows an overall correct code description of target behavior.

II. MONOCHROMATIC IMAGING USING DOUBLE DIFFRACTION OF X RAYS FROM CRYSTALS

In Bragg diffraction from plane crystals, one-dimensional imaging in the direction of dispersion is always obtained. To find the associated spatial resolution (i.e., the minimum resolvable element Δx) we differentiate the Bragg condition $2d\sin\theta=\lambda$ (in first order) to obtain

$$\Delta x = L\tan\theta(\Delta\lambda/\lambda). \tag{4}$$

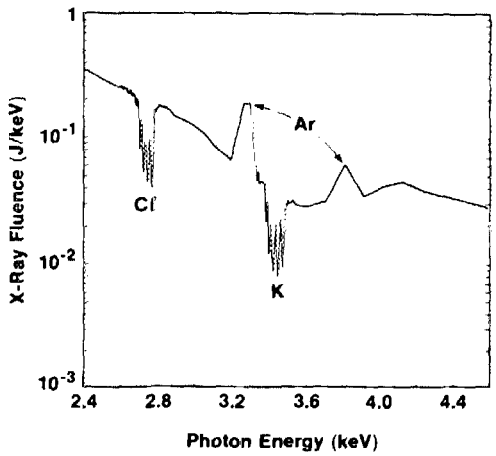

FIG. 5. LASNEX calculated, time-integrated x-ray spectrum emitted from the target, simulating the experiment of Fig. 2.

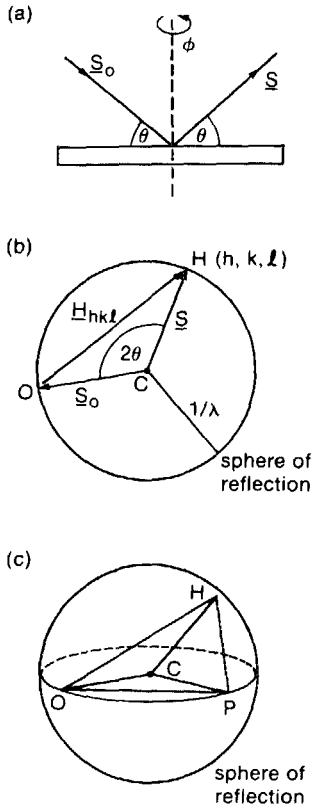

FIG. 6. Schematic of double diffraction. (a) For a monochromatic incident beam, θ is adjusted to the Bragg angle for diffraction from the planes parallel to the surface, and the ϕ rotation brings multiple diffraction peaks into diffraction. (b) Bragg condition in reciprocal lattice (c) by rotating around OH [ϕ rotation in (a)], additional reciprocal lattice points like P touch the reflection sphere.

L is the distance from source to detector along the ray and θ is the Bragg angle. In typical laser-target experiments, this spatial resolution is in fact limited by the spectral width (rather than by the crystal properties). As a typical example we select the Ti^{+20} resonance line at 2.62 Å and assume the laser plasma source to have an ion temperature of 1 keV. The linewidth will be mostly Doppler (with some additional opacity broadening possible), so that $\Delta\lambda/\lambda=3.5\times10^{-4}$, yielding a spatial resolution of 20 μm at $L=10$ cm. In a direction perpendicular to that of the dispersion there is no imaging at all, and the diffracted beam from a divergent source has the shape of a thin conical sheet for a given wavelength.

Double diffraction, by contrast, can provide two-dimensional imaging.[3] The principles of double diffraction are described in Fig. 6. For a monochromatic incoming beam, θ is adjusted to the Bragg angle for diffraction off the planes parallel to the surface. If the structure factor is zero for such diffraction, and the crystal is rotated around the ϕ axis, a series of diffraction peaks appear (such as shown in Figs. 7 and 8). To understand this, we look at the reciprocal-lattice construction, Fig. 6(b). S_0 and S are unit vectors in the direction of the incident and diffracted beams, respectively, and θ is the Bragg angle. The Bragg condition is equivalent to stating that the point H of coordinates (hkl) must lie on the sphere of reflection (or Ewald's sphere): diffraction from the planes of Miller indices (hkl) will then occur along the S direction. If we now rotate the crystal around the ϕ axis, this is equivalent to rotating the reciprocal lattice around OH [Fig. 6(b)]. During this rotation, many points [such as P in Fig. 6(c)] will cross the sphere of reflection and give rise to double diffraction. More than one point can simultaneously cross the sphere, giving rise to multiple-

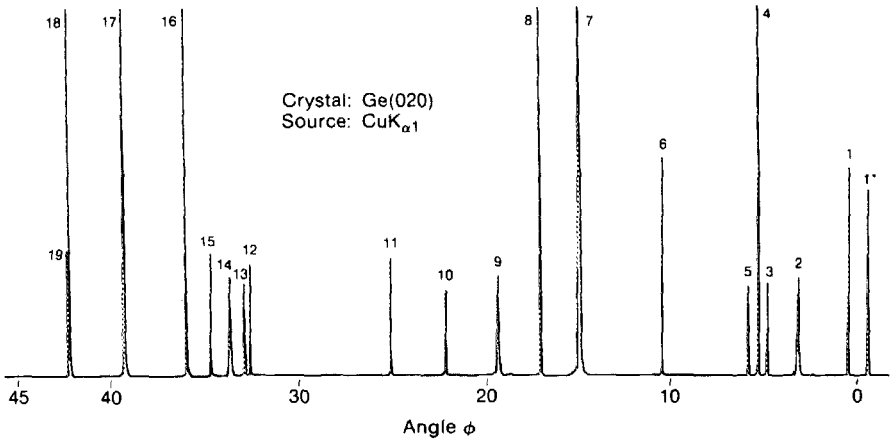

FIG. 7. Double diffraction (three beam) from the (020) planes of germanium. Source: $K\alpha_1$ line of Cu.

beam (such as six-beam) diffraction. In Fig. 6(c), we may say that the incident beam CO is diffracted by the OP planes (i.e., those with Miller indices equal to the coordinates of P), giving rise to a beam diffracted in the CP direction, which is subsequently diffracted by the PH planes (which are perpendicular to PH and are spaced $1/|\mathrm{HP}|$ apart), giving rise to diffraction in the CH direction. Diffraction is in the same direction (CH) as if diffracted from the planes parallel to the surface (OH). In reality, of course, these two diffractions are simultaneous rather than sequential.

Because two angular conditions have to be satisfied (θ and ϕ), the diffracted beam is quasicollimated and can yield a two-dimensional shadowgraph image (of unit magnification), of any object it traverses, or of the emitting object itself.

Multiple diffraction has other important applications,[4] in addition to imaging:

(a) In the Laue mode (radiation traversing the crystal), absorption due to the photoelectric effect is greatly reduced on multiple diffraction peaks. This is in addition to the reduction in absorption (Borrmann effect) in any two-beam Laue diffraction. This property is important for designs of gamma-ray lasers where propagation of wavelengths of order 1 Å through several cm of crystalline material is called for.

(b) The spectral dispersion in this case has two components: $d\theta/d\lambda$, $d\phi/d\lambda$. The second dispersion can be much larger than the first, yielding a high-resolution recording of spectra.

(c) The shape of multiple diffraction peaks near the baseline indicate the sign of the phase shift introduced by the diffraction, thereby enabling the determination of crystal structures from diffraction data.

It should be emphasized that multiple diffracton is not limited to the case of zero structure factor. In the general case, two sets of spectra can appear on the film, with the intersections (enhanced in intensity) corresponding to double diffraction. The two-beam spectra in this case constitute a background for the multiple diffraction peaks.

Figures 7 and 8 show multiple diffraction spectra obtained with Cu $K\alpha_1$ radiation from an x-ray tube. The angle $\phi = 0$ is chosen so that the spectra are mirror imaged with respect to this point. Some of the peaks are higher than the height of the figure and are truncated. The peak marked 7 in Fig. 7 was chosen for the imaging tests in Figs. 9 and 10. It corresponds to simultaneous diffraction from the $(\bar{1}3\bar{1})$ and

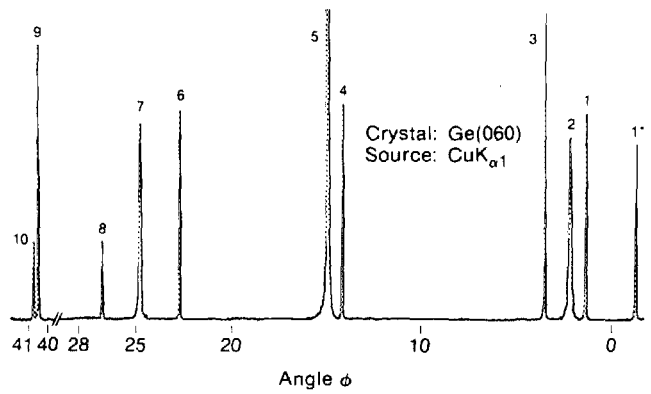

FIG. 8. Double diffraction (three beam) from the (060) planes of germanium. Source: $K\alpha_1$ line of Cu.

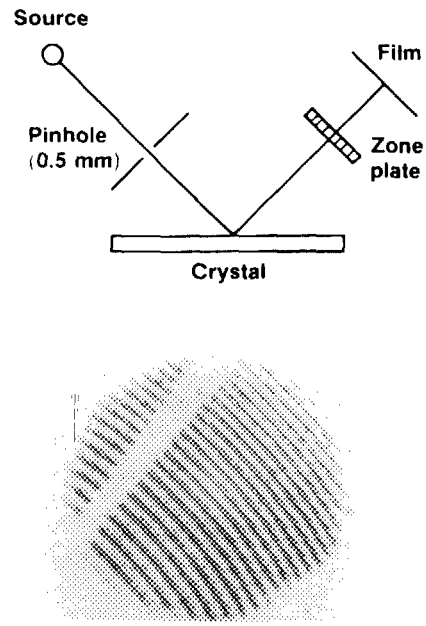

FIG. 9. Imaging testing using the double diffraction peak marked 7 in Fig. 7, from Ge (020) planes. A weak and shifted image due to the $K\alpha_2$ line can be seen.

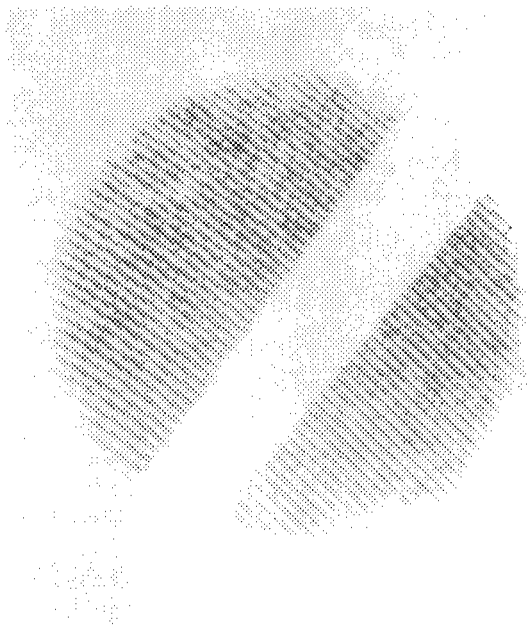

FIG. 10. Imaging of a fine-line section of the zone plate, as in Fig. 9.

$(1\bar{1}1)$ plane sets. The sums of the three indices add up to (020), for this and any double diffraction peak in Fig. 7. This simply follows from the vector relation OH = OP + PH in Fig. 6(c).

Figures 9 and 10 show imaging test results using Cu $K\alpha$ radiation. A free-standing gold zone plate was chosen as a test object to be imaged by shadowgraphy onto a high-resolution film (Kodak RAR-2497). The 0.5-μm pinhole limits the image size and reduces some background, but has no effect on the imaging. The smallest zone-plate linewidth in Fig. 9 is 8 μm, and in Fig. 10 is 5 μm. This is an indication of the spatial resolution achievable in a direction perpendicular to that of the dispersion. In Fig. 9, the distance of source to zone plate (along the ray) is 200 cm, and that of zone plate to film is 2 cm. The source size is about 3 mm, yielding a penumbral shadow of at least 30 μm. Clearly, the imaging in these figures is due to the properties of double diffraction.

The direction of dispersion is seen in Fig. 9, as the $K\alpha_2$ component gives rise to a weak, shifted image with respect to the dominant image. In this direction the spatial resolution is limited by the spectral linewidth, just as in the two-beam Bragg diffraction. As shown above, at a total distance of 10 cm this resolution will be typically 20 μm. In the perpendicular direction the spatial resolution can only be limited by the crystal properties. For the germanium crystal used, the rocking curve width is about 10^{-4}, yielding a spatial resolution of 2 μm for the 2-cm imaging distance in Fig. 9. This agrees with Fig. 10 which indicates a resolution better than 5 μm. In this case the zone plate was rotated by about 90°, to demonstrate the resolution perpendicular to the direction of dispersion. For a total distance of 10 cm from a laser target to the crystal, then to the film, a 10-μm resolution can be achieved in this direction. Different wavelengths will yield images displaced with respect to each other. As shown here, 10–20-μm resolution is possible in a two-dimensionl image at each wavelength. Such images can be useful in studying instability and mixing in laser target implosions. For this, thin layers of elements like titanium or chromium have to be embedded in the target and isolated, strong x-ray lines from the various layers have to be imaged.

ACKNOWLEDGMENTS

This work was supported by the U. S. DOE Office of Inertial Fusion under agreements No. DE-FC08-85DP40200 with the University of Rochester and No. DE-A508-84DP40197 with the Polytechnic Institute of New York. Such support does not imply endorsement of the content by any of the above parties.

[1]A. Hauer, R. D. Cowan, B. Yaakobi, O. Barnouin, and R. Epstein (to be published in Phys. Rev.).
[2]The calculations used in constructing these tables are illustrated in M. F. Argo and W. F. Heubner, J. Quant. Spectrosc. Radiat. Transfer **16**, 1091 (1976).
[3]B. S. Fraenkel, Appl. Phys. Lett. **36**, 341 (1980); **41**, 234 (1982).
[4]B. Post, S. L. Chang, and T. C. Huang, Acta Crystallogr. **A33**, 90 (1977); B. Post, Acta Crystallogr. **A39**, 711 (1983); B. Post, J. Nicholosi, and J. Ladell, Acta Crystallogr. **A40**, 684 (1984).